Article

All-Inorganic Hydrothermally Processed Semitransparent Sb₂S₃ Solar Cells with CuSCN as the Hole Transport Layer

Pankaj Kumar,* Martin Eriksson, Dzmitry S. Kharytonau, Shujie You, Marta Maria Natile, and Alberto Vomiero*

Cite This: ACS Appl. Energy Mater. 2024, 7, 1421−1432

Read Online

ACCESS | Metrics & More | Article Recommendations | Supporting Information

ABSTRACT: An inorganic wide-bandgap hole transport layer (HTL), copper(I) thiocyanate (CuSCN), is employed in inorganic planar hydrothermally deposited Sb₂S₃ solar cells. With excellent hole transport properties and uniform compact morphology, the solution-processed CuSCN layer suppresses the leakage current and improves charge selectivity in an n-i-p-type solar cell structure. The device without the HTL (FTO/CdS/Sb₂S₃/Au) delivers a modest power conversion efficiency (PCE) of 1.54%, which increases to 2.46% with the introduction of CuSCN (FTO/CdS/Sb₂S₃/CuSCN/Au). This PCE is a significant improvement compared with the previous reports of planar Sb₂S₃ solar cells employing CuSCN. CuSCN is therefore a promising alternative to expensive and inherently unstable organic HTLs. In addition, CuSCN makes an excellent optically transparent (with average transmittance >90% in the visible region) and shunt-blocking HTL layer in pinhole-prone ultrathin (<100 nm) semitransparent absorber layers grown by green and facile hydrothermal deposition. A semitransparent device is fabricated using an ultrathin Au layer (∼10 nm) with a PCE of 2.13% and an average visible transmittance of 13.7%.

KEYWORDS: copper(I) thiocyanate, antimony sulfide solar cells, hydrothermal deposition, hole transport layer, semitransparent solar cells, average visible transmittance, thin film solar cells
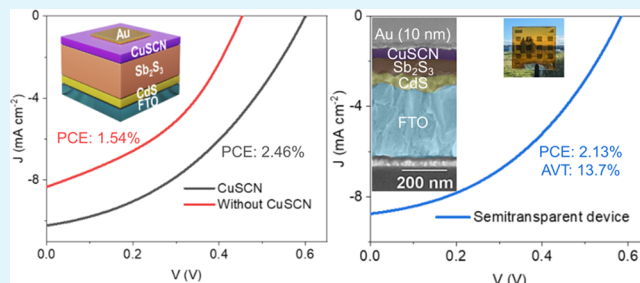
INTRODUCTION

Antimony sulfide (Sb₂S₃) is a promising emerging absorber layer for thin film photovoltaics because of its high absorption coefficient (1.8×10^5 cm^{-1} at 450 nm), suitable optical bandgap [1.7 eV with theoretical Shockley−Queisser limit of power conversion efficiency (PCE) = 28.64%], long-term stability, elemental abundance, and low processing temperatures.[1,2] The relatively high bandgap combined with a high absorption coefficient makes it a potential candidate for semitransparent solar cell applications.

Sb₂S₃ has a relatively low doping concentration and thus has a quasi-intrinsic nature. Doping Sb₂S₃ is difficult due to its ribbon-like crystal structure.[3] An n-i-p-type structure, with an electron transport layer (ETL, n-type) and hole transport layer (HTL, p-type), can effectively relax the requirement on the doping density of the Sb₂S₃ absorber layer.[4] The built-in electric field n-i-p solar cell is defined by the Fermi level difference between the ETL and HTL and charge extraction is expected to improve.[4] The top-performing Sb₂S₃ solar cells in recent years employ an n-i-p planar device structure with maximum PCE exceeding 8%.[5,6]

An organic small molecule, 2,2′,7,7′-tetrakis(*N,N*-di-*p*-methoxyphenylamine)-9,9′-spiro-fluorene (Spiro-OMeTAD), or a polymer, poly(3-hexylthiophene-2,5-diyl) (P3HT), have

been the materials of choice as HTL in the most efficient Sb₂S₃ solar cells.[5,7−9] In general, these expensive organic HTLs suffer from inherent chemical and thermal instability. Therefore, considerable research efforts have been devoted to the search for suitable inorganic HTL materials.[10,11] Among these inorganic HTLs, CuSCN is a cheaper, thermally stable alternative with sufficient hole mobility and transparency. Additionally, CuSCN has suitable properties to act as efficient HTL with a wide bandgap (E_g) of ∼3.6 eV, suitable field-effect mobility values reported up to 0.4 cm² V^{-1} s^{-1}, and matched energy levels with Sb₂S₃ (valence band, $E_v = -5.4$ eV with respect to vacuum).[12−14]
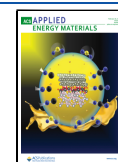
The efficiencies remained lower than 2% for planar Sb₂S₃ solar cells with CuSCN as the HTL layer.[15] In comparison, those using Spiro-OMeTAD as HTL have achieved a PCE of 8%.[5] The major limitation in Sb₂S₃ solar cells comes from high voltage loss ($V_{loss} = E_g/e - V_{OC}$, where E_g is the bandgap of the

light absorbing semiconductor, e is the elementary electronic charge, and V_{OC} is the open circuit voltage), which is more than 0.9 V for state-of-the-art Sb_2S_3 solar cells based on Spiro-OMeTAD.[5] In comparison, the top-performing silicon and perovskite solar cells have achieved V_{loss} as low as 0.3−0.5 V.[16] For CuSCN-based planar Sb_2S_3 devices, the V_{OC} values are even lower.[15] Therefore, considering the promising physical and optoelectronic characteristics, CuSCN needs more investigation and optimization, especially targeting improvement in V_{OC}.

In our previous work,[15] CuSCN showed promising results in planar all-inorganic Sb_2S_3 solar cells where the absorber layer was deposited via chemical bath deposition (CBD). The devices with the structure $FTO/TiO_2/Sb_2S_3/CuSCN/Au$ achieved a PCE of 1.75%. One of the major limitations of the device's performance was the low-quality nonuniform Sb_2S_3 film produced by CBD with oxygen impurities and unfavorable crystal orientations. Thus, the optimum thickness of Sb_2S_3 was limited to ~50 nm with island-like morphology resulting in unavoidable HTL/ETL direct contacts.[15] In recent years, planar Sb_2S_3 solar cells based on an alternative green and facile solution-based approach (the hydrothermal deposition method) have consistently achieved PCEs higher than 6% (albeit with Spiro-OMeTAD as HTL).[6,17,18] In this work, to further improve the performance, a fully inorganic planar hydrothermally processed Sb_2S_3 solar cell based on CuSCN as the HTL is reported. A detailed optoelectronic characterization of CuSCN for HTL applications is followed by the simulation of solar cell devices with and without CuSCN. In the fabricated devices, the PCE of the solar cell with CuSCN HTL (device structure: $FTO/CdS/Sb_2S_3/CuSCN/Au$) was improved by up to 60% in comparison to the device without HTL. The obtained PCE of 2.46% is one of the highest among previously reported CuSCN-based planar Sb_2S_3 solar cells. Moreover, the inclusion of the CuSCN layer becomes even more consequential when the thickness of the Sb_2S_3 layer is reduced to below 100 nm. In these ultrathin Sb_2S_3 solar cells, the devices with the CuSCN HTL maintain high V_{OC} even at a thickness of 60 nm because of the shunt-blocking effect of the CdS/CuSCN heterojunction. On the other hand, the HTL-free devices are highly shunted for Sb_2S_3 thickness below 100 nm. These results suggest that CuSCN is a promising, cheaper, and stable alternative to expensive and inherently unstable organic HTLs. Furthermore, as demonstrated, the hydrothermal method can produce ultrathin Sb_2S_3 films for semitransparent solar cell applications. Thus, a proof-of-concept semitranspar-ent device (with a 10 nm Au top electrode) is reported with a PCE of 2.13% and an average visible transmittance (AVT) of 13.7%.

■ EXPERIMENTAL SECTION

Device fabrication: FTO substrates (TEC 15) were cleaned using Hellmanex III solution (2 vol % in distilled water), distilled water, acetone, and isopropanol, respectively, for 10 min each, followed by drying in an oven for 10 min at 120 °C. A CdS layer was deposited following a conventional CBD recipe.[19] The deposition time was adjusted to achieve a thickness of 70−80 nm. Sb_2S_3 films were deposited using a hydrothermal deposition method. 0.02 M potassium antimonyl tartrate trihydrate (≥99%, VWR chemicals) and 0.08 M sodium thiosulfate pentahydrate (>99.5%, VWR chemicals) were added to a 30 mL Teflon lined autoclave. The hydrothermal reaction was carried out for varying times (60−240 min) at 135 °C according to ref 18. The coated films were rinsed in distilled water and annealed in a tube furnace in argon at 350 °C (ramp rate 10 °C per min) for 10

min.[18] CuSCN was spin-coated from a diethyl sulfide at 4000 rotations per min (rpm) and dried at 90 °C for 10 min, following our previous report.[15] Au top contact was sputtered using a compact sputter coater (Leica EM ACE200) and the device area was defined by a laser-cut metal mask with an area of 9 mm². For a space charge limited current (SCLC) device, NiO_x hole injection contact was prepared via spin coating following previously reported recipes.[20,21] Briefly, 276.3 mg of $Ni(NO_3)_2 \cdot 6H_2O$ was dissolved in 2-methoxyethanol (10 mL). After the mixture was stirred at 50 °C for 1 h, 100 µL of acetylacetone was added to the solution. After stirring for 1 h, the solution was filtered through a nylon filter (0.45 µm) and spin-coated on FTO at 3000 rpm and further annealed in air at 150 °C for 1 h. Control devices using an organic HTL P3HT (Ossila, M108) were prepared using the following conditions: a concentration of 10 mg mL^{-1} in chlorobenzene, spin-coated at 4000 rpm, and annealed in a tube furnace in an argon atmosphere at 120 °C for 10 min. To improve the contact with Au, a diluted (1:6 volume ratio in isopropanol) PEDOT:PSS (Ossila PH1000) was subsequently spin-coated on PEDOT:PSS at 2000 rpm and annealed in a tube furnace in the argon atmosphere at 120 °C for 10 min.[9,22]

Characterization and Measurements. *Optical Character-ization.* Transmittance/absorbance characterizations were performed by a Cary 5000 spectrophotometer. The optical bandgap, E_g, of thin films, was extracted using Tauc's formula: $(\alpha h\nu)^\gamma = C (h\nu − E_g)$, where α is the absorption coefficient, $h\nu$ is the photon energy, C is a constant, and γ takes the values of 2 or 1/2 for direct and indirect bandgap, respectively.[23] The absorption coefficient, α was calculated using the equation: $\alpha = A\ln10/t$, where A is the absorbance and t is the thickness of the film (determined by cross-section scanning electron microscopy (SEM).[24] For both Sb_2S_3 and CuSCN films, both direct ($\gamma = 2$) and indirect ($\gamma = 1/2$) bandgaps were extracted from the Tauc plots. Both direct and indirect bandgaps have been calculated based on the previous reports for CuSCN[25] and Sb_2S_3[26] thin films. AVT was calculated using the equation:[27]

$$ AVT = \frac{\int T(\lambda) \times V(\lambda) \times AM1.5G(\lambda)d\lambda}{\int V(\lambda) \times AM1.5G(\lambda)d\lambda} $$

where λ is the wavelength, $T(\lambda)$ is the transmission spectrum with air as a reference, $V(\lambda)$ is the photopic response of the human eye, and AM1.5G represents the standard solar photon flux.

SCLC Mobility Characterization. In hole-only SCLC devices, the current varies linearly at low voltages, followed by a SCLC regime (assuming a trap-free semiconductor film) where the current is proportional to V^2. In this SCLC regime, the Mott−Gurney equation[28] was used to calculate the hole mobility, μ_h, given by

$$ J = \frac{9}{8}\varepsilon_r\varepsilon_0\mu_h\frac{V^2}{L^3} $$

where ε_0 is the permittivity of free space, $\varepsilon_r = 5.1$,[29] which is the dielectric constant of CuSCN, V is the voltage, and L is the thickness of the film (~100 nm). The thickness of CuSCN can be tuned simply by changing the spin-coating speed (Figure S1).

SEM Morphology and Cross-Section. Morphology and cross sections of films and devices were characterized by Magellan 400 Field Emission Scanning Electron Microscopy.

X-ray diffraction patterns (XRD) were collected on a PANalytical Empyrean X-ray diffractometer with a Cu K$_\alpha$ source.

Atomic Force Microscopy (AFM) and Kelvin Probe Force Microscopy (KPFM). The AFM topography maps and KPFM contact potential difference (CPD) maps were recorded using an NTEGRA system from NT-MDT Spectrum Instruments. High-quality top-ography maps were recorded in semicontact mode using cantilever A on a HA_NC tip from NT-MDT with a nominal force constant of 12 N/m. The CPD was recorded with 2-pass KPFM in ambient conditions using an ElectriTap300-G tip from BudgetSensors having a nominal force constant of 40 N/m. For the thin films on FTO, conductive HQ:NSC18/Pt probes from µmasch with a nominal force constant of 2.8 N/m were used. The freshly sputtered Pt and Au samples were used as potential references and examined before and
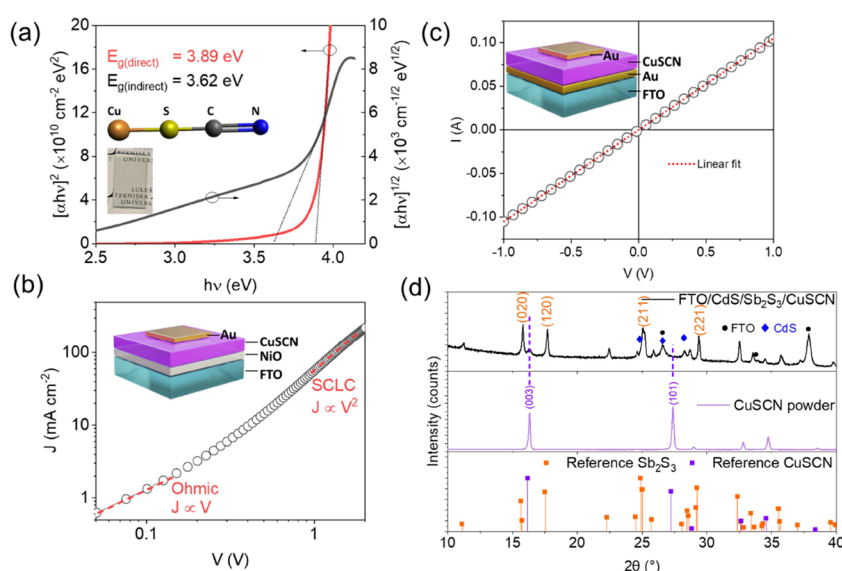
Figure 1. (a) Plots of $(\alpha h\nu)^{1/2}$ and $(\alpha h\nu)^2$ calculated for the CuSCN film. The inset shows a 60 nm CuSCN film coated on an FTO substrate. (b) $J-V$ curves for SCLC devices showing the ohmic and SCLC region. The device structure is also shown. (c) $I-V$ curve for conductivity measurement along with the device structure. (d) X-ray diffraction pattern of commercial CuSCN powder and the annealed CuSCN film on the Sb_2S_3 film. The reference patterns are also plotted for peak matching.

after every measurement. During the second pass, the cantilever was lifted 100 nm above the sample surface, and the amplitude of the applied AC voltage was 3 V. The sample substrate was connected to the ground during the entire measurement.

X-ray Photoelectron Spectroscopy (XPS). XPS analysis was performed with a ThermoFisher Escalab QXi spectrometer using monochromatic Al $K\alpha$ radiation and argon-assisted charge compensation. All signal positions are given in terms of binding energy. Both extended (survey: pass energy of 100 eV; dwell time of 20 ms; step of 1 eV) and detailed spectra (pass energy of 25 eV; dwell time of 50 ms; step of 0.1 eV) were collected. Spectra were analyzed with ThermoFisher Advantage software (2023 version). All quantifications were performed from detailed spectra.

Device Characterizations. The current density–voltage ($J-V$) measurements were performed using a Keithley 2400 source meter under simulated AM 1.5G irradiation (100 mW cm^{-2}) with a standard 100 W Xe lamp-based solar simulator Oriel LCS-100 (default scan parameters: forward scan from -0.2 to 0.8 V; scan rate: 100 mV/s). The illumination intensity was calibrated by a monocrystalline silicon reference cell (Oriel 91150) P/N). The external quantum efficiency (EQE) was measured using the Rera SpeQuest quantum efficiency system, calibrated by silicon solar cell reference. Electrical impedance spectroscopy (EIS) measurements were performed using an electrochemical workstation (Solartron Analytical, ModulabXM) in the frequency range from 1 MHz to 1 Hz with an applied potential of 0.6 V in the dark. Equivalent circuit fitting was performed using an EIS Spectrum Analyzer developed by Bondarenko et al.[30]

SCAPS Simulation. A numerical simulation program, SCAPS-1D, developed by Burgelman et al., was used to simulate the device structure.[31] The simulated structures consist of FTO/CdS/Sb_2S_3/CuSCN or P3HT/Au or HTL-free FTO/CdS/Sb_2S_3/Au. Equations governing the simulation software are described in Supplementary Note 1. The parameters and material properties are listed in Table S1, along with the corresponding references. The comparison with the reported literature is given in Table S2. The output of the simulations (along with nonideal conditions as discussed in Supplementary Note 2) are shown in Table S3 and Figure S2.

■ RESULTS AND DISCUSSION

Material Characterization. The absorption spectra of CuSCN and Sb_2S_3 films are shown in Figure S3a. The CuSCN layer is quite transparent (average transmittance >90% in the

300−800 nm range with an AVT of 93.5%) in the absorption region of Sb_2S_3 (Figure S3b), which is quite attractive for semitransparent and tandem Sb_2S_3 solar cells.[32] Since there is no consensus in the literature about the type of bandgap (direct or indirect) for CuSCN,[33] Tauc plots were used to extract both direct ($E_{g\text{-direct}}$) and indirect ($E_{g\text{-indirect}}$) optical bandgaps (Figure 1a). The CuSCN film showed a good straight-line fit for both direct and indirect types of optical transitions. The calculated $E_{g\text{-direct}}$ and $E_{g\text{-indirect}}$ were 3.89 and 3.62 eV, respectively, close to those reported elsewhere.[12,34] The presence of an indirect E_g in CuSCN thin films has been linked to the observation of a long tail region in the absorption spectrum.[25] Similarly, the direct and indirect optical bandgaps of Sb_2S_3 were ca. 1.76 and 1.58 eV, respectively, as reported elsewhere as direct[35] or both direct and indirect[26,36] (Figure S3c). Moreover, both direct and indirect bandgaps for Sb_2S_3 were predicted in DFT simulations.[26] For thin film solar absorber applications, a direct bandgap type material is preferred because of its more efficient absorption around the bandgap.[37] To evaluate the hole transport properties of the CuSCN films, hole-only mobility was calculated in a SCLC device with a device configuration (FTO/NiO/CuSCN/Au, Figure 1b). Both FTO/NiO and Au should make ohmic contact with CuSCN to ensure efficient hole injection.[38] Hence, KPFM was used to determine the work function (WF) of these films.[39] The morphology and CPD of CuSCN (70 and 200 nm) and NiO films on FTO are shown in Figure S4a−f. The measured work functions of these films (NiO: -5.09 eV, CuSCN-200 nm: -5.27 eV, and CuSCN-70 nm: -5.32 eV) are close to that of Au (taken as the reference with the WF of -5.1 eV) and confirm the p-type character of these films (NiO valence band: -5.4 eV).[21] Notably, the work functions of CuSCN films were weakly dependent on the thickness or roughness of the films, which would ensure spatially uniform hole conduction properties (Figure S4g). The cross-sectional image of the SCLC device is also shown in Figure S4h. The hole mobility (μ_h) was calculated in the SCLC regime as 1.74 (± 0.61) $\times 10^{-4}$ cm^2 V^{-1} s^{-1}. This value is lower than those

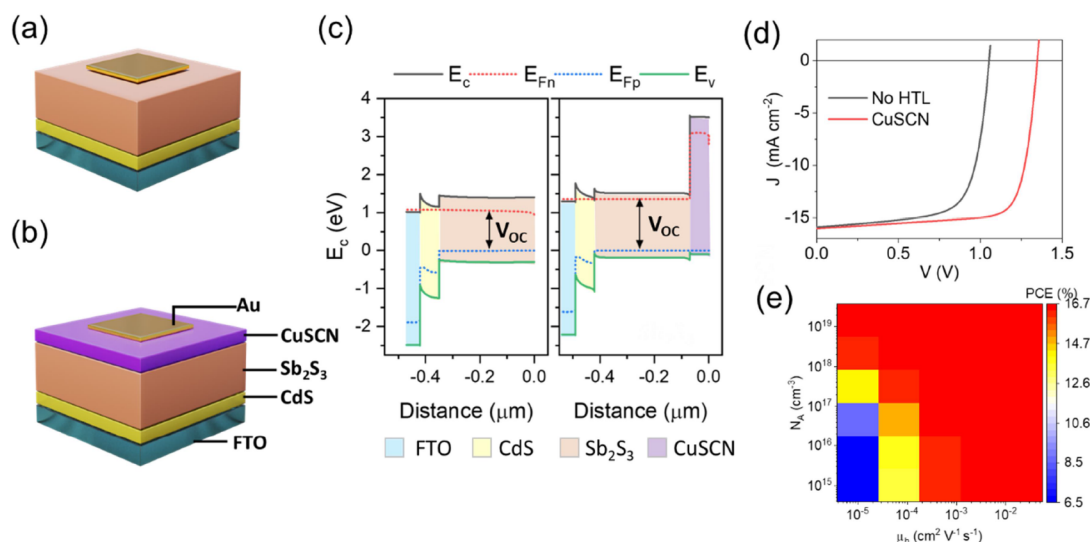**Figure 2.** Device architecture of the planar Sb_2S_3 solar cell (a) without and (b) with CuSCN HTL. (c) Energy band diagrams of CdS/Sb_2S_3 and $CdS/Sb_2S_3/CuSCN$ devices under AM1.5G irradiation at open circuit conditions. (d) Simulated $J-V$ curves of the two cases: with and without CuSCN layer. (e) Contour plot for variation of PCE of the devices with acceptor density (N_A) and hole mobility (μ_h) of CuSCN HTL.

reported by other measurement techniques such as field-effect mobility $(0.1 \; \text{cm}^2 \; \text{V}^{-1}\text{s}^{-1})$[12] or time-of-flight $(\sim 10^{-3} \; \text{cm}^2 \; \text{V}^{-1}\text{s}^{-1})$.[40] However, SCLC mobility is more realistic for solar cell application since the film thickness is the same range as the solar cell (the time-of-flight technique uses films in μm thickness range) and the mobility is calculated across the thickness of the film (in contrast to field-effect mobility, where mobility is calculated in in-plane direction).[40] To measure the conductivity and verify the nature of CuSCN/Au contact (ohmic or Schottky), a device with the structure FTO/Au/CuSCN/Au was prepared (Figure 1c). An ohmic contact was formed between CuSCN and Au, which is important for efficient charge extraction and reduction of the recombination losses. The conductivity (σ) was calculated as $1.1 \; (\pm 0.02) \times 10^{-5} \; \Omega^{-1} \; \text{cm}^{-1}$ from the ohmic slope of the $I-V$ plot, $I = \sigma(A/d)V$,[41] where A is the device area $(0.09 \; \text{cm}^2)$ and d is the thickness of the CuSCN layer measured using SEM cross-section images (Figure S4h). Using the mobility and conductivity values, a carrier concentration of $3.95 \; (\pm 0.12) \times 10^{17} \; \text{cm}^{-3}$ is calculated using the equation $\sigma = N_A e \mu_h$, where N_A is the carrier density of acceptors in CuSCN, e is the elementary charge, and σ is the conductivity of the film. This is consistent with the values reported elsewhere.[29,42]

The XRD from the $FTO/CdS/Sb_2S_3/CuSCN$ stack is studied and reported in Figure 1d. In the middle panel in Figure 1d, the diffraction patterns from the commercial CuSCN powder match well with reference JCPDS #29-0581, which confirms its β-phase structure. Furthermore, the weak peak at 16.1° in Figure 1d top panel is assigned to the (003) diffraction from the CuSCN film (60−70 nm) coated on Sb_2S_3. The strongest diffraction peaks below 35° are assigned to the orthorhombic Sb_2S_3 (JCPDS #42-1393, space group Pbnm).[36] $[hk1]$-oriented crystal is known to have relatively rapid transport of photogenerated carriers and higher performance compared to $[hk0]$-orientation.[43] The presence of $[hk1]$-oriented peaks such as (221) and (211) along with $[hk0]$-oriented peaks such as (120) and (020) suggest that there was no preferential orientation in the hydrothermally deposited Sb_2S_3 films.

Device Simulation. Although CuSCN has been successfully applied in perovskite solar cells, the reports of its application in planar Sb_2S_3 solar cells are limited.[44,45] Moreover, there are several reports of high-performance Sb_2S_3 solar cells without the HTL layer ("HTL-free").[46,47] Therefore, drift-diffusion simulations for solar cell devices with and without CuSCN as the HTL were performed to study the theoretical influence of the addition of an HTL layer on the device performance in an n-i-p configuration. Figure 2a,b show the device structures without and with the HTL layer. Figure 2c shows the energy level diagrams for these devices under open circuit conditions under 1 sun illumination. The corresponding simulated $J-V$ curves are shown in Figure 2d, with the material parameters fixed as in Table S1. The device without an HTL suffers from low V_{OC} and FF but comparable J_{SC} values (with CuSCN: PCE = 16.48%, V_{OC} = 1.35 V, J_{SC} = 16.04 mA cm^{-2}, FF = 76.20%; Without HTL: PCE = 11.75%, V_{OC} = 1.05 V, J_{SC} = 15.91 mA cm^{-2}, and FF = 70.08%). The addition of CuSCN with a higher conduction band (E_c) (than that of Sb_2S_3 as represented in Figure 2c) suppresses the electron back transfer from Sb_2S_3 to top contact (Au) and reduces the charge recombination, thus increasing the FF. The theoretical maximum V_{OC} is defined as the quasi-Fermi-level splitting (QFLS) (inside the absorber layer) between the electron and hole Fermi levels ($E_{Fn} - E_{Fp}$, represented by black and blue dotted lines in Figure 2c).[48] Introducing CuSCN increases the selectivity of electrons and holes and thus reduces the level of recombination near the hole contact. On the other hand, without the CuSCN HTL, the quasi-Fermi level of electrons is further reduced near the top contact (here Au with work function (WF = −5.1 eV) was used). Thus, the net effect of CuSCN is an increase in the QFLS, thus increasing the V_{OC}.[48]

However, since CuSCN will also add additional resistance, conductivity, which is a product of mobility and acceptor carrier concentration (doping density, N_A) becomes an important parameter. Thus, the hole mobility (μ_h) and acceptor carrier density (N_A) are two of the most important parameters that influence the effectiveness of the HTL. It is also possible to tune these properties using doping or other
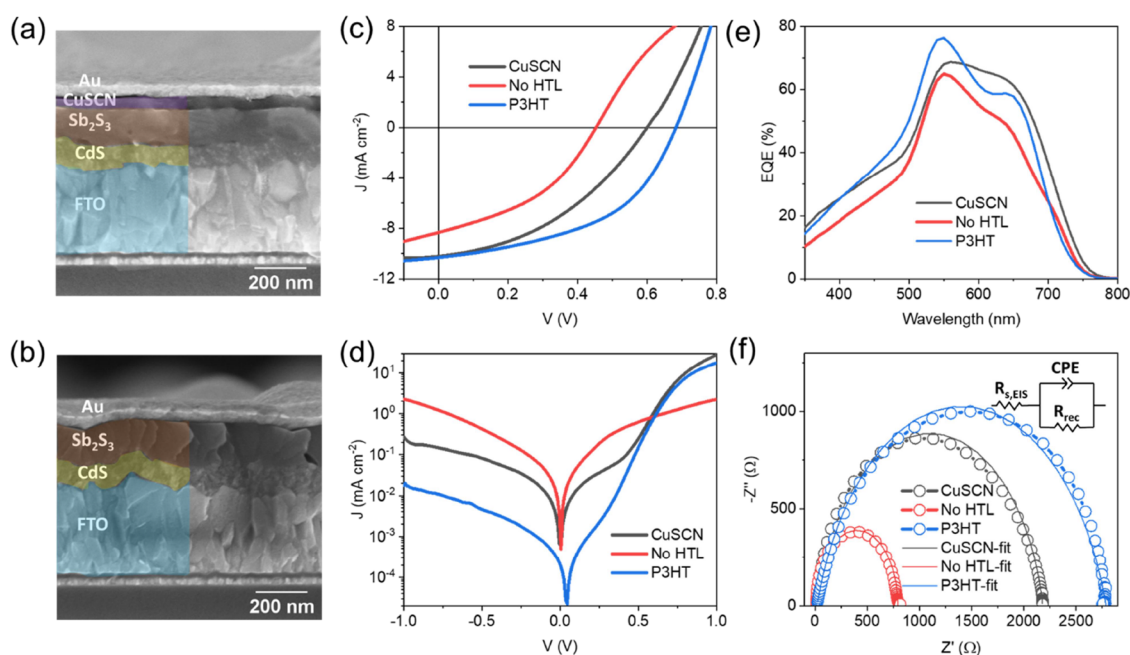
Figure 3. Cross-sectional SEM image of a typical solar cell (a) with and (b) without a CuSCN HTL. (c) Light $J-V$ curves, (d) dark $J-V$ curves, (e) external quantum efficiency of solar cells, and (f) Nyquist plots for devices with CuSCN and P3HT HTLs and without HTL.

Table 1. Device Performance Parameters of Solar Cell Devices With and Without a CuSCN HTL

		V_{OC} (V)	J_{SC} (mA cm^{-2})	FF (%)	PCE (%)	R_s (Ω cm^2)	R_{sh} (Ω cm^2)
CuSCN	best	0.60	10.22	40.13	2.46	24.5	347.2
	mean $\pm$ SD[a]	0.62 $\pm$ 0.02	8.86 $\pm$ 0.85	41.9 $\pm$ 1.89	2.30 $\pm$ 0.09	27.4 $\pm$ 2.7	340.3 $\pm$ 38.5
no HTL	best	0.45	8.36	40.63	1.54	21.7	134.9
	mean $\pm$ SD[a]	0.42 $\pm$ 0.03	8.30 $\pm$ 0.22	38.40 $\pm$ 1.84	1.35 $\pm$ 0.18	23.7 $\pm$ 1.4	118.9 $\pm$ 14.3
P3HT	best	0.68	10.34	48.41	3.42	15.2	317.5
	mean $\pm$ SD[a]	0.68 $\pm$ 0.05	10.07 $\pm$ 0.27	48.24 $\pm$ 0.40	3.31 $\pm$ 0.10	15.0 $\pm$ 0.5	317.3 $\pm$ 16.1

[a]Mean and standard deviation (SD) calculated from the average of the top 6 devices for CuSCN and P3HT-based devices and 5 devices for no-HTL devices. The thicknesses of the absorber layers are as follows: 200 nm for CuSCN-based devices, 260 nm for no-HTL devices, and 110−120 nm for P3HT devices. CuSCN layer was 60−70 nm thick and P3HT (with PEDOT:PSS modification layer) was about 30−40 nm.

post-treatments of CuSCN.[14,49] A contour plot showing the effect of varying these two parameters (other parameters are the same as Table S1) is plotted in Figure 2e. The PCE of devices based on the CuSCN HTL layer is highly sensitive at lower values of both μ_h and N_A and saturates beyond certain minimum values ($\mu_h > 10^{-4}$ cm^2 V^{-1}s^{-1} and $N_A > 10^{17}$ cm^{-3}). These values are quite achievable in CuSCN thin film without doping as in the current investigation and reported elsewhere.[29,50] Furthermore, a comparison table of reported simulations of planar Sb$_2$S$_3$ solar with different device structures is presented in Table S2. The device with a CuSCN HTL in the ideal case (low bulk defect density of 10^{12} cm^{-3} and no interface traps) should theoretically perform as well as other HTLs. Some selected experimental reports are also listed. V_{OC} loss is the major loss factor in the experimental devices compared with the simulations.

Photovoltaic Performance. The cross-sectional SEM images of the typical devices with and without CuSCN HTL are shown in Figure 3a,b, respectively. The compact CuSCN film is in intimate contact with the Sb$_2$S$_3$ layer. The top surface SEM and AFM images of Sb$_2$S$_3$ before and after CuSCN coating are shown in Figure S5a−d. CuSCN film showed full coverage of Sb$_2$S$_3$ film, filling the pinholes in the films. With conformal and compact coverage, CuSCN would reduce the shunt paths and leakage currents in the solar cells.[51] Notably,

the pinholes (morphology) were not taken into consideration in the SCAPS simulated devices but would determine the property of physical contact with the top electrode, especially for the solution-processed Sb$_2$S$_3$ layer with noncompact morphology with pinholes.[52]

Figure 3c shows the $J-V$ curves of champion Sb$_2$S$_3$ solar cells with and without the CuSCN HTL layer along with P3HT HTL as a control reference device.[53] The corresponding photovoltaic performance parameters are listed in Table 1, and the thicknesses of Sb$_2$S$_3$ and HTLs are given in the footnote. The statistical distribution of these solar cells is shown in Figure S6. Higher reproducibility is clearly an added advantage of adding CuSCN (the mean and standard deviation of all the parameters are listed in Table 1). The thickness of CuSCN was optimized by varying the spin-coating RPMs (Figure S1a−c), and the corresponding device performance parameters are listed in Table S4. The champion device with CuSCN obtained a PCE of 2.46% (V_{OC} = 0.60 V, J_{SC} = 10.22 mA cm^{-2}, and FF = 40.13%). A typical forward and reverse scan showed less than 5% hysteresis (Figure S7), suggesting efficient charge transfer across the device. The champion device without an HTL showed a PCE of 1.54% (V_{OC} = 0.45 V, J_{SC} = 8.36 mA cm^{-2}, and FF = 40.63%). The reference device with P3HT showed both higher V_{OC} and FF, resulting in a PCE of 3.42%. Sb$_2$S$_3$ and P3HT have been reported to form an

intimate chelating bonding contact and it possibly passivates the interface.[54]

The efficiencies of these HTL-free devices are lower compared to the literature with similar device structures (FTO/CdS/Sb_2S_3/Au, with reported PCEs over 5%) which points to the room for potential improvements in the PCEs via optimization of ETL and Sb_2S_3 processing conditions.[46,47] With the aim of shedding light on the possible causes of the lower performances of these devices with respect to most planar Sb_2S_3 solar cells with similar structures reported in the literature, X-ray photoelectron spectroscopic analysis was carried out on the FTO/CdS/Sb_2S_3. Besides confirming the growth of Sb_2S_3, the XPS analysis also revealed a significant presence of Sb_2O_3 on the surface (Figure S8 and Supplementary Note 3), which is detrimental to the device performance as reported elsewhere.[36,55] Choi et al.[56] reported a high concentration of deep defects (up to 5×10^{14} cm^{-3} at 0.52 eV above the valence band) due to oxide impurities. Furthermore, low performances can be attributed to the discontinuous morphology with pinholes and smaller grains (<500 nm) compared to dense morphology in the reported literature for hydrothermally deposited Sb_2S_3 films.[57] Moreover, as shown in the energy-dispersive X-ray spectroscopy (EDS) measurements (Figure S9), the atomic ratio of S/Sb for Sb_2S_3 films on FTO is 1.45, suggesting that the Sb_2S_3 film is S-deficient. Sulfur vacancy (V_s) also contributes to deep traps and associated recombination losses.[57]

Consequently, a huge discrepancy exists between the simulated and experimental data. To make the simulations more realistic and to understand the effects of nonidealities, three nonideal cases were added to the device simulation one by one. The "ideal" case represents the baseline simulation in Figure 2d. In the subsequent simulations, actual device parameters and deep and interface defects were introduced (Supplementary Note 2). The effects of these nonidealities can be seen in calculated J−V curves (Figure S2) and Table S3. The results are consistent with our conclusion that the HTL layer plays a significant role in improving the performance and limiting the shunts. The limitation of these 1-D simulations in replicating the actual devices is also discussed briefly in Supplementary Note 2.

The rollover effect (S-shape in the J−V curve Figure 3c) can be seen in the device without the HTL layer, which is characteristic of the top contact barrier (nonohmic contact).[58] Without the HTL layer, the Sb_2S_3 interface would form a Schottky contact with Au, which will act in a reverse direction to the main junction (CdS/Sb_2S_3), reducing the V_{OC}. This observation is well established and a selenization treatment would often solve the nonohmic Sb_2S_3/Au contact, by lowering the E_g (Sb_2Se_3 formation) at the HTL interface.[52,59] Series and shunt resistances of the two devices in light were calculated from the linear slopes near open circuit ($1/R_s = dJ/dV|_{V=Voc}$) and short circuit ($1/R_{sh} = dJ/dV|_{V=0\ V}$) conditions, respectively.[60] Average R_s of the devices with no HTL was slightly lower than that of the device with CuSCN (23.7 ± 1.4 Ω cm^2 for no HTL vs 27.4 ± 2.7 Ω cm^2 for CuSCN-based devices). However, the shunt resistance for the CuSCN device is much higher (340.3 ± 38.5 Ω cm^2) compared to that of the device without the HTL layer (118.9 ± 14.3 Ω cm^2). Higher shunt resistance achieved by employing the CuSCN HTL layer means reduced leakage currents and thus a higher average FF and V_{OC}. P3HT-based devices showed both lower R_s and higher R_{sh}. Serious leakage currents and a lack of selectivity

(low rectification ratio) can be seen in the dark J−V curves without HTL along with a lack of diode rectification characteristics (Figure 3d). The dark reverse current is significantly reduced signifying the role of HTL (CuSCN or P3HT) in improving the charge selectivity. The shallow conduction band of both the HTLs (−1.5 eV for CuSCN and −3.2 eV for P3HT)[36] reduces the electron injection from Au to Sb_2S_3 and vice versa.[61]

The short circuit current density, $J_{SC,}$ is influenced by the absorption, charge separation, and collection properties of the device in the absence of an externally applied field. To study the wavelength-dependent charge collection efficiency of the solar cells, EQE measurements were carried out (Figure 3e). The integrated $J_{SC,EQE}$ values were close to those measured via the solar simulator (9.00 mA cm^{-2} for no-HTL device, 11.07 mA cm^{-2} for the CuSCN device, and 10.81 mA cm^{-2} for the P3HT device). A relative improvement in EQE in CuSCN and P3HT-based devices in higher wavelength regions (>600 nm) can be attributed to lower shunt losses (as seen in low leakage currents in dark J−V curves in Figure 3d) along with better hole collection (electron reflection) efficiency of the hole contact since the electron−hole pairs are created near the hole contact for long-wavelength photons and electrons can easily recombine with Au contact in absence of the electron blocking HTL. In the low wavelength regions (<500 nm), the improvement in EQE of both HTL-based devices can be attributed to efficient hole extraction. In this low wavelength region, photons are completely absorbed near the CdS/Sb_2S_3 interface. The generated electrons and holes formed near the electron contact are separated by the built-in electric field and collected by CdS and hole contact, respectively. The built-in potentials can be estimated from crossover point of light and dark J−V curves as shown in Figure S10.[62] Electrons can be easily collected by CdS since they are created near the CdS layer, while the holes need to travel through the low Sb_2S_3 absorber layer to the hole contact (Au or HTL/Au). Introduction of an HTL reduces the Schottky barrier (evidenced by S-shaped rollover in J−V in Figure 3c), increases built-in potential (0.46, 0.66, and 0.75 V, respectively for no HTL, CuSCN, and P3HT-based devices as shown in Figure S10), reduces the shunt losses (lower leakage currents in dark J−V in Figure 3d), and possibly improves the hole extraction rate due to favorable band alignment.[51,63]

Furthermore, charge transport and recombination characteristics of the cells with and without CuSCN HTL were studied by using electrical impedance spectroscopy measurements (EIS) in the dark (Figure 3f). The Nyquist plot showed a single depressed semicircle, which is modeled by a series resistance component, $R_{S,EIS}$ (combining all resistances including that of electrodes) in series with a parallel combination of recombination resistance (R_{rec})—constant phase element, CPE. $R_{S,EIS}$ value for the device in the dark without HTL (12.4 vs 20.0 Ω) is lower than that with CuSCN, while the R_{rec} for the CuSCN device is substantially higher. With CuSCN HTL, R_{rec} has increased (from 780 to 2161 Ω), implying reduced recombination in the device and, thus higher V_{OC}. P3HT device showed further improved recombination resistance (2750 Ω) possibly due to its passivating contact with P3HT.[9,54] Since the n-sides of the devices (CdS/Sb_2S_3) and WFs of electrodes are identical in all cases, these R_{rec} values are primarily associated with the hole contact properties.

Surface Potential. To further investigate the improvement of device performance (especially the V_{OC}), surface potentials
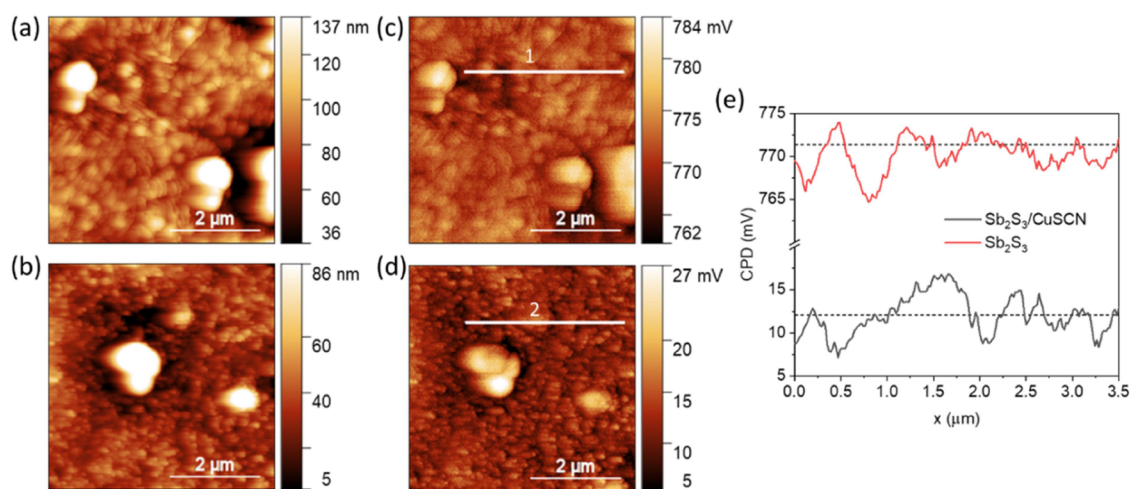
Figure 4. AFM topography maps of (a) hydrothermally deposited Sb_2S_3 and (b) CuSCN coated on the Sb_2S_3 film and their corresponding KPFM maps: (c) Sb_2S_3 and (d) Sb_2S_3/CuSCN film. (e) Line profile of the surface potential of (c) and (d) along lines 1 and 2, shown inside the CPD scans, respectively.
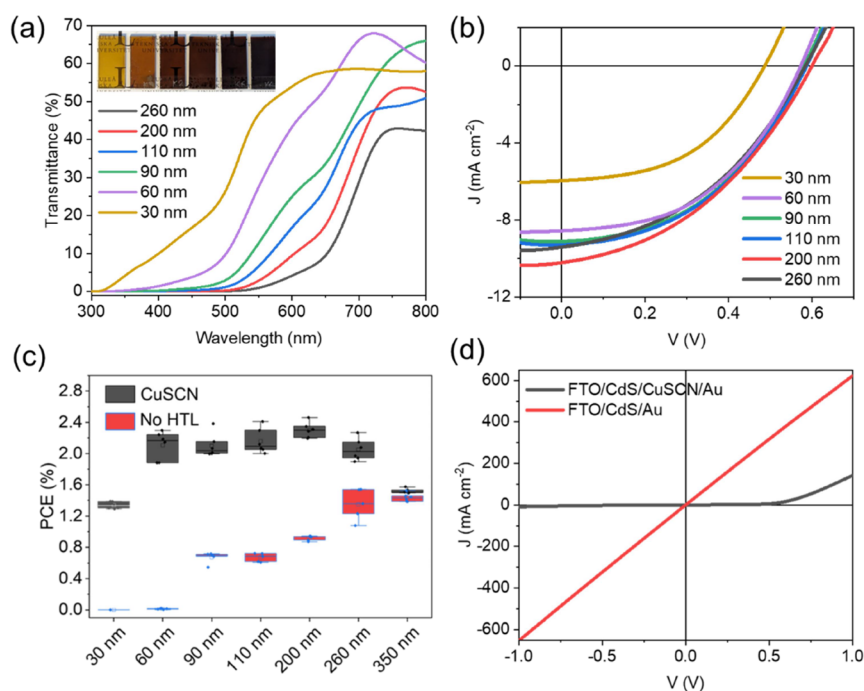

Figure 5. (a) Transmittance of FTO/CdS/Sb_2S_3/CuSCN stacks with varying thicknesses of the Sb_2S_3 absorber layer. The inset shows photographs of these stacks: the thickness of Sb_2S_3 increases from left (30 nm) to right (260 nm). (b) Performance parameters of devices (FTO/CdS/Sb_2S_3/CuSCN/Au) with varying thicknesses of absorber layers. (c) Thickness vs PCE variation of devices with and without CuSCN HTL layer. (d) $J-V$ curves of devices representing direct contact between electron and hole contacts. FTO/CdS/Au and FTO/CdS/CuSCN/Au represent the pinhole areas (with no Sb_2S_3 layer) of the solar cells without and with the CuSCN HTL layer.

before and after CuSCN deposition on Sb_2S_3 were mapped using KPFM. The variations in CPD between the tip and the sample, across the entire scan area (including grain boundaries and morphology as shown in Figure 4a,b) are below 10 mV for both films (Figure 4c,d). This fluctuation is lower than the thermal energy per electron (kT/e = 25.7 mV, where k is the Boltzmann constant, T is temperature, and e is the elementary charge) (Figure 4e). This indicates that the CuSCN was deposited conformally on the Sb_2S_3 (covering even the subμm sized hemispherical grains of Sb_2S_3) and the electrical properties do not vary across the film. The CPD of CuSCN film on Sb_2S_3 (12.1 ± 0.7 mV) translates to an average WF

value (E_F) of −5.08 eV (calibrated against the Au electrode with a WF of −5.10 eV). The deviation of the WF of CuSCN films on Sb_2S_3 (∼0.2 eV) from those on the FTO substrates (Figure S4g) can be attributed to slightly different laboratory conditions (temperature and humidity), which might affect the measurement. The measured values for E_F of CuSCN are in close agreement with previous reports.[12,64] Similarly, the work function of Sb_2S_3 (−4.32 eV) is close to the middle of the bandgap (considering E_v = −5.72 eV,[65] and E_g = 1.76 eV), suggesting a weak n-type character. The obtained work function value is close to the previously reported value.[66] Moreover, the measured WF values CuSCN films (−5.08 to
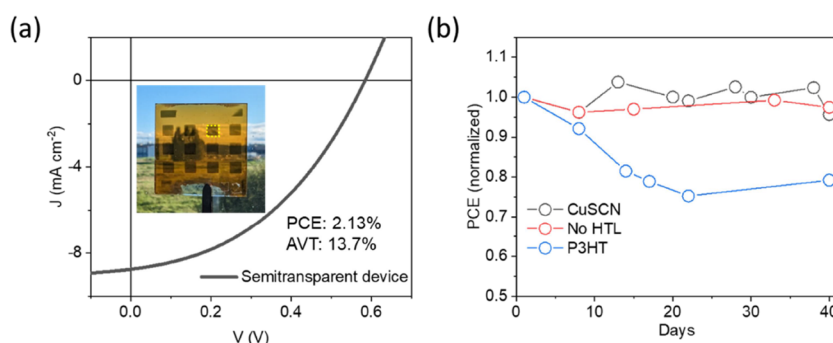
Figure 6. (a) $J-V$ curve of a semitransparent Sb_2S_3 solar cell. The inset shows a photograph of the devices on a 25×25 mm^2 substrate. The yellow dotted lines mark the device area (darker shade) with ~10 nm Au electrode. (b) Variations of PCE in shelf-life stability testing of unencapsulated devices stored in the dark at an RH of 30−50% and a temperature of 20−26 °C.

−5.32 eV) are close to the valence band ($E_v = -5.4$ eV),[12] suggesting a p-type character with high carrier density ($>10^{17}$ cm^{-3}).[50]

Another important attribute of employing CuSCN with a high E_F (and E_v) is the elimination of the Fermi-level pinning phenomenon. Savadogo and Mandal[67] reported that the Schottky barrier height was independent of the work function of the top contact and concluded the Fermi level was pinned near the midgap of Sb_2S_3 (around −4.5 eV). Hence, isolating the Sb_2S_3 layer from top contact via a CuSCN HTL eliminates a major V_{OC}-limiting phenomenon (Fermi-level pinning) because of its high E_F.

Semitransparent Solar Cells. Sb_2S_3 has a wide bandgap and high absorption coefficient (10^5 cm^{-1}); and therefore, it is a potential candidate for semitransparent and tandem solar cell applications.[32] To this end, CuSCN with its high optical transparency (ultrawide bandgap of ~3.9 eV) is favorably suitable as the HTL. To achieve sufficient semitransparency (of at least 25% for commercial applications), the thickness of the absorber layer must be reduced to less than 100 nm.[53] The thickness of the absorber layer can be tuned by tuning the duration of the hydrothermal film deposition, as shown in Figure S11. The transmittance curves of the devices without the top contact layer (FTO/CdS/Sb_2S_3/CuSCN) are shown in Figure 5a, achieving high AVTs of 45.7 and 30.4% with 30 and 60 nm Sb_2S_3 absorber layers, respectively (AVT values are listed in Table S5). The $J-V$ curves of the corresponding CuSCN-based devices with varying absorber thicknesses are shown in Figure 5b, and the performance parameters are listed in Table S5. The thickness reduction results in a higher probability of direct contact between electron and hole contacts via pinholes as shown in Figure S12 (arrows indicate the shunt paths in the ~60 nm thick absorber layer). These shunt pathways lead to drastically decreased FF and V_{OC} in devices without CuSCN (as shown in Figure S13 and Table S6). P3HT has a similar shunt-reducing effect as seen in the PCE vs thickness trend in Figure S14a. The corresponding device performance parameters are listed in Table S7. The $J-V$ curves (with varying Sb_2S_3 thicknesses) and cross-section SEM image of a typical P3HT device are shown in Figure S14b,c, respectively. As evident from the statistical distribution of PCEs vs thicknesses (Figure 5c), devices without the HTL layer did not perform at all until Sb_2S_3 thickness was increased to at least 90 nm. On the other hand, devices utilizing the CuSCN layer achieved a decent relative performance (compared to the device with the optimum thickness of 200 nm with a PCE of 2.46% as discussed earlier) with a PCE of

2.30% at 60 nm. Unfortunately, this pinhole shunt effect is not taken into account in the 1-D device simulation discussed earlier. The reason for the increased tolerance to shunts in ultrathin absorber layers can be found in the nature and magnitude of leakage currents in the regions where pinholes occur. Direct contact of CdS ETL with Au (FTO/CdS/Au) results in a very low shunt resistance (calculated from the slope at $V = 0$ V) of 1.6 Ω cm^2 (Figure 5d). In contrast, it is increased by 2 orders of magnitude to 336 Ω cm^2 upon insertion of a CuSCN layer (FTO/CdS/CuSCN/Au). Therefore, the parallel shunt current (created due to direct contact between the electron and hole contacts) is significantly more detrimental in the absence of the CuSCN layer. In addition, a nonohmic diode-like $J-V$ characteristic for ETL-HTL devices has been reported to be more tolerant to shunts (pinholes) compared to an ohmic shunt path since the leakage currents are very low below the turn-on voltage (around 0.5 V).[68] In summary, the CuSCN layer screens the detrimental effects of the two-dimensional variations in the thickness (and shunts) of the ultrathin Sb_2S_3 absorber film. A semitransparent proof-of-concept device with ultrathin Au electrode (~10 nm based on the previous report)[53] showed a PCE of 2.13% at an AVT of 13.7% (Figure 6a and Table S8). The cross-section SEM image is shown in Figure S15a, and the transmittance curves of the device with and without an Au electrode are shown in Figure S15b. The AVT of the device was reduced by more than 50% (from 30.4% for the 60 nm Sb_2S_3 absorber layer without the Au electrode) to 13.7% due to the low transmittance of the Au electrode.[53] In comparison, due to the low AVT of P3HT (59.4%), FTO/CdS/Sb_2S_3 (60 nm)/P3HT shows an AVT of merely 9.0% (Figure S15b). This AVT loss can be reduced by employing an alternative top electrode with higher transparency (e.g., graphene as the transparent top electrode with more than 80% transmittance in the visible region, as reported by Zhang et al.[32]). The AVT of the device stack can be further improved by replacing CdS (AVT = 74.9%) with wide bandgap ETLs, such as TiO$_2$ (AVT = 90.0%) (transmission spectra of these films are shown in Figure S3b).

Stability. Solar cell devices integrating the CuSCN-based HTL show much better stability than those based on organic HTLs.[44,51] The evolution performance parameters of devices without and with HTLs are shown in Figure 6b. The CuSCN-based device retained 96% of its initial PCE, after 40 days of ambient storage (similar to that without the HTL layer). In contrast, the P3HT-based device retained only 79% of its PCE. CuSCN is intrinsically stable and highly stable perovskite solar cells based on CuSCN have been reported frequently.[44,45]

CuSCN-based planar Sb_2Se_3 also showed excellent ambient shelf stability.[69] However, despite these promising results, there is a need to investigate the photostability under continuous illumination under ambient (and controlled humid) conditions for these planar Sb_2S_3 solar cells.

CONCLUSIONS

In summary, a low-temperature solution-processed HTL, CuSCN was utilized in hydrothermally deposited planar Sb_2S_3 solar cells. The optoelectronic properties of CuSCN for HTL applications were studied in detail. Material parameters influencing the hole transport characteristics of the CuSCN HTL and their effects on the device performance were simulated using drift-diffusion simulation software (SCAPS-1D). The simulation predicted increased V_{OC} and FF, with the addition of CuSCN as the HTL layer. Consistent with the simulation, in the devices, the CuSCN layer provided a high work function hole conducting-electron blocking layer between the Sb_2S_3 absorber and Au electrode and thus suppressed reverse leakage currents and improved recombination resistance. Devices with CuSCN HTL show a PCE ∼60% higher than those without the HTL (PCE of 2.46 vs 1.54%). CuSCN-based planar Sb_2S_3 devices have traditionally shown low PCEs in the limited number of reports in the literature, and this is one of the best-performing devices in the literature (Table S9) along with room for improvement via optimization of ETL and Sb_2S_3 layers. In addition, devices with semitransparent absorbers with thicknesses as low as 60 nm (AVT of 30.4% without top Au electrode) maintained decent performances of 2.30% in an opaque device and 2.13% in the corresponding semitransparent device (with AVT of 13.7% using ∼10 nm Au) because of the shunt-blocking properties of CuSCN HTL. These results show that CuSCN is a promising low-cost HTL candidate for all-inorganic planar semitransparent Sb_2S_3 solar cells based on a green and facile hydrothermal deposition.

ASSOCIATED CONTENT

Ⓢ Supporting Information

The Supporting Information is available free of charge at https://pubs.acs.org/doi/10.1021/acsaem.3c02492.

SEM cross sections showing CuSCN thickness variations with spin coating speeds; details about SCAPS-1D simulation software; electrical parameters of layers used in SCAPS-1D simulation; literature reports of simulated and experimental results of planar Sb_2S_3 solar cells; a brief description of nonidealities and corresponding simulated solar cell performance parameters in ideal and nonideal cases for CuSCN, P3HT, and no-HTL devices; absorption/transmittance spectrum of Sb_2S_3, CuSCN, CdS, TiO_2, and P3HT films; KPFM images and work function data of CuSCN and NiO films on FTO; cross-section image of hole-only SCLC device; SEM and AFM images of the top surfaces of Sb_2S_3 and Sb_2S_3/CuSCN; PCE performance variation vs thicknesses of CuSCN HTL; statistics of device performance parameters for devices with CuSCN, no-HTL, and P3HT; forward and reverse $J-V$ curves of a typical CuSCN-based device; XPS and EDS spectra and analysis of Sb_2S_3 films; $J-V$ curves showing dark and light crossover; cross-section images of $FTO/CdS/Sb_2S_3$ stacks with varying hydrothermal deposition times (varying Sb_2S_3 thicknesses);

cross-section images of CuSCN-based and no-HTL devices utilizing 60 nm Sb_2S_3 layers; $J-V$ curves of devices without HTL layers with varying Sb_2S_3 thicknesses; statistical distribution of PCE (with varying thicknesses of Sb_2S_3), $J-V$ curves (with varying thicknesses of Sb_2S_3) and a typical SEM cross-section image of P3HT-based devices; PCE variation with varying thicknesses of Sb_2S_3 absorber for CuSCN, P3HT, and no-HTL-based devices; typical SEM cross-section image of CuSCN-based semitransparent device; transmittance and AVTs of the semitransparent device along with $FTO/CdS/Sb_2S_3/CuSCN$ or P3HT stacks without the top electrode; device performance parameters of semitransparent device; and literature reports of CuSCN-based planar solar cells (PDF)

AUTHOR INFORMATION

Corresponding Authors

Pankaj Kumar — *Division of Materials Science, Department of Engineering Sciences and Mathematics, Luleå University of Technology, SE-971 87 Luleå, Sweden;* ⓞ orcid.org/0000-0002-1853-214X; Email: pankaj.kumar@ltu.se

Alberto Vomiero — *Division of Materials Science, Department of Engineering Sciences and Mathematics, Luleå University of Technology, SE-971 87 Luleå, Sweden; Department of Molecular Sciences and Nanosystems, Ca' Foscari University of Venice, 30172 Venezia Mestre, Italy;* ⓞ orcid.org/0000-0003-2935-1165; Email: alberto.vomiero@ltu.se

Authors

Martin Eriksson — *Division of Materials Science, Department of Engineering Sciences and Mathematics, Luleå University of Technology, SE-971 87 Luleå, Sweden*

Dzmitry S. Kharytonau — *Electrochemistry and Corrosion Laboratory, Jerzy Haber Institute of Catalysis and Surface Chemistry, Polish Academy of Sciences, 30-239 Krakow, Poland*

Shujie You — *Division of Materials Science, Department of Engineering Sciences and Mathematics, Luleå University of Technology, SE-971 87 Luleå, Sweden;* ⓞ orcid.org/0000-0001-7475-6394

Marta Maria Natile — *National Research Council (CNR), Institute of Condensed Matter Chemistry and Technologies for Energy (ICMATE), 35131 Padova, Italy; Department of Chemical Sciences, University of Padova, 35131 Padova, Italy;* ⓞ orcid.org/0000-0001-5591-2670

Complete contact information is available at:
https://pubs.acs.org/10.1021/acsaem.3c02492

Author Contributions

P.K.: conceptualization, methodology, investigation, writing original draft, and formal analysis. M.E.: AFM and KPFM measurements, formal analysis. D.S.K.: AFM and KPFM measurements. M.M.N.: XPS, formal analysis, and review. S.Y.: supervision and review. A.V.: supervision, review, and editing. All authors have given approval to the final version of the manuscript.

Notes

The authors declare no competing financial interest.

■ REFERENCES

(1) Rühle, S. Tabulated Values of the Shockley—Queisser Limit for Single Junction Solar Cells. *Sol. Energy* **2016**, *130*, 139−147.

(2) Zimmermann, E.; Pfadler, T.; Kalb, J.; Dorman, J. A.; Sommer, D.; Hahn, G.; Weickert, J.; Schmidt-Mende, L. Toward High-Efficiency Solution-Processed Planar Heterojunction Sb2S3 Solar Cells. *Advanced Science* **2015**, *2* (5), No. 1500059.

(3) Ishaq, M.; Deng, H.; Farooq, U.; Zhang, H.; Yang, X.; Shah, U. A.; Song, H. Efficient Copper-Doped Antimony Sulfide Thin-Film Solar Cells via Coevaporation Method. *Solar RRL* **2019**, *3* (12), No. 1900305.

(4) Chen, C.; Tang, J. Open-Circuit Voltage Loss of Antimony Chalcogenide Solar Cells: Status, Origin, and Possible Solutions. *ACS Energy Lett.* **2020**, *5* (7), 2294−2304.

(5) Wang, S.; Zhao, Y.; Che, B.; Li, C.; Chen, X.; Tang, R.; Gong, J.; Wang, X.; Chen, G.; Chen, T.; Li, J.; Xiao, X. A Novel Multi-Sulfur Source Collaborative Chemical Bath Deposition Technology Enables 8%-Efficiency Sb2S3 Planar Solar Cells. *Adv. Mater.* **2022**, *34* (41), No. 2206242.

(6) Chen, S.; Li, M.; Zhu, Y.; Cai, X.; Xiao, F.; Ma, T.; Yang, J.; Shen, G.; Ke, A.; Lu, Y.; Liang, W.; Hsu, H.-Y.; Chen, C.; Tang, J.; Song, H. A Codoping Strategy for Efficient Planar Heterojunction Sb2S3 Solar Cells. *Adv. Energy Mater.* **2022**, *12* (47), No. 2202897.

(7) Han, J.; Pu, X.; Zhou, H.; Cao, Q.; Wang, S.; He, Z.; Gao, B.; Li, T.; Zhao, J.; Li, X. Synergistic Effect through the Introduction of Inorganic Zinc Halides at the Interface of TiO2 and Sb2S3 for High-Performance Sb2S3 Planar Thin-Film Solar Cells. *ACS Appl. Mater. Interfaces* **2020**, *12* (39), 44297−44306.

(8) Jiang, C.; Tang, R.; Wang, X.; Ju, H.; Chen, G.; Chen, T. Alkali Metals Doping for High-Performance Planar Heterojunction Sb2S3 Solar Cells. *Solar RRL* **2019**, *3* (1), No. 1800272.

(9) Gao, J.; Tang, R.; Cai, H.; Cai, Z.; Xiao, P.; Li, G.; Jiang, C.; Zhu, C.; Chen, T. Oriented Organization of Poly(3-Hexylthiophene) for Efficient and Stable Antimony Sulfide Solar Cells. *ENERGY & ENVIRONMENTAL MATERIALS* **2023**, *6*, No. e12453.

(10) Jin, X.; Yuan, Y.; Jiang, C.; Ju, H.; Jiang, G.; Liu, W.; Zhu, C.; Chen, T. Solution Processed NiOx Hole-Transporting Material for All-Inorganic Planar Heterojunction Sb2S3 Solar Cells. *Sol. Energy Mater. Sol. Cells* **2018**, *185*, 542−548.

(11) Zhang, L.; Jiang, C.; Wu, C.; Ju, H.; Jiang, G.; Liu, W.; Zhu, C.; Chen, T. V2O5 as Hole Transporting Material for Efficient All Inorganic Sb2S3 Solar Cells. *ACS Appl. Mater. Interfaces* **2018**, *10* (32), 27098−27105.

(12) Wijeyasinghe, N.; Regoutz, A.; Eisner, F.; Du, T.; Tsetseris, L.; Lin, Y.-H.; Faber, H.; Pattanasattayavong, P.; Li, J.; Yan, F.; McLachlan, M. A.; Payne, D. J.; Heeney, M.; Anthopoulos, T. D. Copper(I) Thiocyanate (CuSCN) Hole-Transport Layers Processed from Aqueous Precursor Solutions and Their Application in Thin-Film Transistors and Highly Efficient Organic and Organometal Halide Perovskite Solar Cells. *Adv. Funct. Mater.* **2017**, *27* (35), No. 1701818.

(13) Singh, R.; Singh, P. K.; Bhattacharya, B.; Rhee, H.-W. Review of Current Progress in Inorganic Hole-Transport Materials for Perovskite Solar Cells. *Applied Materials Today* **2019**, *14*, 175−200.

(14) Baig, S.; D. Hendsbee, A.; Kumar, P.; Ahmed, S.; Li, Y. Yttrium-Doped CuSCN Thin Film Transistor: Synthesis and Optoelectronic Characterization Study. *J. Mater. Chem. C* **2019**, *7* (46), 14543−14554.

(15) Kumar, P.; You, S.; Vomiero, A. CuSCN as a Hole Transport Layer in an Inorganic Solution-Processed Planar Sb2S3 Solar Cell, Enabling Carbon-Based and Semitransparent Photovoltaics. *J. Mater. Chem. C* **2022**, *10* (43), 16273−16282.

(16) Lian, W.; Tang, R.; Ma, Y.; Wu, C.; Chen, C.; Wang, X.; Fang, F.; Zhang, J.; Wang, Z.; Ju, H.; Zhu, C.; Chen, T. Probing the Trap States in N−i−P Sb2(S,Se)3 Solar Cells by Deep-Level Transient Spectroscopy. *J. Chem. Phys.* **2020**, *153* (12), 124703.

(17) Huang, Y.; Gao, H.; Peng, X.; Wang, G.; Xiao, P.; Che, B.; Tang, R.; Zhu, C.; Chen, T. A Robust Hydrothermal Sulfuration Strategy Towards Effective Defect Passivation Enabling 6.92% Efficiency Sb₂S₃ Solar Cells. *Sol. RRL* **2023**, *7*, No. 2201115, DOI: 10.1002/solr.202201115.

(18) Tang, R.; Wang, X.; Lian, W.; Huang, J.; Wei, Q.; Huang, M.; Yin, Y.; Jiang, C.; Yang, S.; Xing, G.; Chen, S.; Zhu, C.; Hao, X.; Green, M. A.; Chen, T. Hydrothermal Deposition of Antimony Selenosulfide Thin Films Enables Solar Cells with 10% Efficiency. *Nature Energy* **2020**, *5* (8), 587−595.

(19) Qi, Y.; Li, Y.; Lin, Q. Engineering the Charge Extraction and Trap States of Sb2S3 Solar Cells. *Appl. Phys. Lett.* **2022**, *120* (22), 221102.

(20) Jung, J. W.; Chueh, C.-C.; Jen, A. K.-Y. A Low-Temperature, Solution-Processable, Cu-Doped Nickel Oxide Hole-Transporting Layer via the Combustion Method for High-Performance Thin-Film Perovskite Solar Cells. *Adv. Mater.* **2015**, *27* (47), 7874−7880.

(21) Liu, Z.; Chang, J.; Lin, Z.; Zhou, L.; Yang, Z.; Chen, D.; Zhang, C.; Liu, S. F.; Hao, Y. High-Performance Planar Perovskite Solar Cells Using Low Temperature, Solution−Combustion-Based Nickel Oxide Hole Transporting Layer with Efficiency Exceeding 20%. *Adv. Energy Mater.* **2018**, *8* (19), No. 1703432.

(22) Kim, D.-H.; Lee, S.-J.; Park, M. S.; Kang, J.-K.; Heo, J. H.; Im, S. H.; Sung, S.-J. Highly Reproducible Planar Sb2S3-Sensitized Solar Cells Based on Atomic Layer Deposition. *Nanoscale* **2014**, *6* (23), 14549−14554.

(23) Chen, C.; Li, W.; Zhou, Y.; Chen, C.; Luo, M.; Liu, X.; Zeng, K.; Yang, B.; Zhang, C.; Han, J.; Tang, J. Optical Properties of Amorphous and Polycrystalline Sb₂Se₃ Thin Films Prepared by Thermal Evaporation. *Appl. Phys. Lett.* **2015**, *107* (4), No. 043905.

(24) Li, Y.; Yan, W.; Li, Y.; Wang, S.; Wang, W.; Bian, Z.; Xiao, L.; Gong, Q. Direct Observation of Long Electron-Hole Diffusion Distance in CH3NH3PbI3 Perovskite Thin Film. *Sci. Rep* **2015**, *5* (1), 14485.

(25) Pattanasattayavong, P.; Promarak, V.; Anthopoulos, T. D. Electronic Properties of Copper(I) Thiocyanate (CuSCN). *Advanced Electronic Materials* **2017**, *3* (3), No. 1600378.

(26) Guo, L.; Zhang, B.; Li, S.; Zhang, Q.; Buettner, M.; Li, L.; Qian, X.; Yan, F. Scalable and Efficient Sb2S3 Thin-Film Solar Cells Fabricated by Close Space Sublimation. *APL Materials* **2019**, *7* (4), No. 041105.

(27) Lee, K.; Um, H.-D.; Choi, D.; Park, J.; Kim, N.; Kim, H.; Seo, K. The Development of Transparent Photovoltaics. *Cell Reports Physical Science* **2020**, *1* (8), No. 100143.

(28) Goh, C.; Kline, R. J.; McGehee, M. D.; Kadnikova, E. N.; Fréchet, J. M. J. Molecular-Weight-Dependent Mobilities in Regioregular Poly(3-Hexyl-Thiophene) Diodes. *Appl. Phys. Lett.* **2005**, *86* (12), 122110.

(29) Pattanasattayavong, P.; Mottram, A. D.; Yan, F.; Anthopoulos, T. D. Study of the Hole Transport Processes in Solution-Processed Layers of the Wide Bandgap Semiconductor Copper(I) Thiocyanate (CuSCN). *Adv. Funct. Mater.* **2015**, *25* (43), 6802−6813.

(30) Bondarenko, A. S.; Ragoisha, G. A. *Progress in Chemometrics Research*; Nova Science: New York, 2005; pp 1110−1112 (http://www.abc.chemistry.bsu.by/vi/).

(31) Burgelman, M.; Nollet, P.; Degrave, S. Modelling Polycrystalline Semiconductor Solar Cells. *Thin Solid Films* 2000, 361−362, 527−532.

(32) Zhang, J.; Lian, W.; Yin, Y.; Wang, X.; Tang, R.; Qian, C.; Hao, X.; Zhu, C.; Chen, T. All Antimony Chalcogenide Tandem Solar Cell. *Solar RRL* 2020, 4 (4), No. 2000048.

(33) Pattanasattayavong, P.; Yaacobi-Gross, N.; Zhao, K.; Ndjawa, G. O. N.; Li, J.; Yan, F.; O'Regan, B. C.; Amassian, A.; Anthopoulos, T. D. Hole-Transporting Transistors and Circuits Based on the Transparent Inorganic Semiconductor Copper(I) Thiocyanate (CuSCN) Processed from Solution at Room Temperature. *Adv. Mater.* 2013, 25 (10), 1504−1509.

(34) Jaffe, J. E.; Kaspar, T. C.; Droubay, T. C.; Varga, T.; Bowden, M. E.; Exarhos, G. J. Electronic and Defect Structures of CuSCN. *J. Phys. Chem. C* 2010, 114 (19), 9111−9117.

(35) Medina-Montes, M. I.; Montiel-González, Z.; Paraguay-Delgado, F.; Mathews, N. R.; Mathew, X. Structural, Morphological and Spectroscopic Ellipsometry Studies on Sputter Deposited Sb2S3 Thin Films. *J. Mater. Sci: Mater. Electron* 2016, 27 (9), 9710−9719.

(36) Kondrotas, R.; Chen, C.; Tang, J. Sb2S3 Solar Cells. *Joule* 2018, 2 (5), 857−878.

(37) Kangsabanik, J.; Svendsen, M. K.; Taghizadeh, A.; Crovetto, A.; Thygesen, K. S. Indirect Band Gap Semiconductors for Thin-Film Photovoltaics: High-Throughput Calculation of Phonon-Assisted Absorption. *J. Am. Chem. Soc.* 2022, 144 (43), 19872−19883.

(38) Sajedi Alvar, M.; Blom, P. W. M.; Wetzelaer, G.-J. A. H. Space-Charge-Limited Electron and Hole Currents in Hybrid Organic-Inorganic Perovskites. *Nat. Commun.* 2020, 11 (1), 4023.

(39) Singh, A.; Gupta, S. K.; Garg, A. Inkjet Printing of NiO Films and Integration as Hole Transporting Layers in Polymer Solar Cells. *Sci. Rep* 2017, 7 (1), 1775.

(40) Mohan, L.; Ratnasingham, S. R.; Panidi, J.; Daboczi, M.; Kim, J.-S.; Anthopoulos, T. D.; Briscoe, J.; McLachlan, M. A.; Kreouzis, T. Determining Out-of-Plane Hole Mobility in CuSCN via the Time-of-Flight Technique To Elucidate Its Function in Perovskite Solar Cells. *ACS Appl. Mater. Interfaces* 2021, 13 (32), 38499−38507.

(41) Heo, J. H.; Im, S. H. CH3NH3PbI3/Poly-3-Hexylthiophen Perovskite Mesoscopic Solar Cells: Performance Enhancement by Li-Assisted Hole Conduction. *physica status solidi (RRL) −. Rapid Research Letters* 2014, 8 (10), 816−821.

(42) Kavan, L.; Živcová, Z. V.; Hubík, P.; Arora, N.; Dar, M. I.; Zakeeruddin, S. M.; Grätzel, M. Electrochemical Characterization of CuSCN Hole-Extracting Thin Films for Perovskite Photovoltaics. *ACS Appl. Energy Mater.* 2019, 2 (6), 4264−4273.

(43) Jin, X.; Fang, Y.; Salim, T.; Feng, M.; Hadke, S.; Leow, S. W.; Sum, T. C.; Wong, L. H. In Situ Growth of [Hk1]-Oriented Sb2S3 for Solution-Processed Planar Heterojunction Solar Cell with 6.4% Efficiency. *Adv. Funct. Mater.* 2020, 30 (35), No. 2002887.

(44) Arora, N.; Dar, M. I.; Hinderhofer, A.; Pellet, N.; Schreiber, F.; Zakeeruddin, S. M.; Grätzel, M. Perovskite Solar Cells with CuSCN Hole Extraction Layers Yield Stabilized Efficiencies Greater than 20%. *Science* 2017, 358 (6364), 768−771.

(45) Liu, J.; Pathak, S. K.; Sakai, N.; Sheng, R.; Bai, S.; Wang, Z.; Snaith, H. J. Identification and Mitigation of a Critical Interfacial Instability in Perovskite Solar Cells Employing Copper Thiocyanate Hole-Transporter. *Advanced Materials Interfaces* 2016, 3 (22), No. 1600571.

(46) Pawar, P. S.; Nandi, R.; Rao Eswar Neerugatti, K.; Sharma, I.; Kumar Yadav, R.; Tae Kim, Y.; Yu Cho, J.; Heo, J. Atomic-Layer-Deposited TiO2 and SnO2 Coupled with CdS as Double Buffer Layers for HTL-Free Sb2S3 Thin-Film Solar Cells. *Sol. Energy* 2022, 246, 141−151.

(47) Zeng, Y.; Huang, J.; Li, J.; Sun, K.; Shah, U. A.; Deng, H.; Zhang, X.; Sha, C.; Qian, C.; Song, H.; Hao, X. Comparative Study of TiO2 and CdS as the Electron Transport Layer for Sb2S3 Solar Cells. *Solar RRL* 2022, 6, No. 2200435.

(48) Caprioglio, P.; Stolterfoht, M.; Wolff, C. M.; Unold, T.; Rech, B.; Albrecht, S.; Neher, D. On the Relation between the Open-Circuit Voltage and Quasi-Fermi Level Splitting in Efficient Perovskite Solar Cells. *Adv. Energy Mater.* 2019, 9 (33), No. 1901631.

(49) Perera, V. P. S.; Senevirathna, M. K. I.; Pitigala, P. K. D. D. P.; Tennakone, K. Doping CuSCN Films for Enhancement of Conductivity: Application in Dye-Sensitized Solid-State Solar Cells. *Sol. Energy Mater. Sol. Cells* 2005, 86 (3), 443−450.

(50) Sun, J.; Zhang, N.; Wu, J.; Yang, W.; He, H.; Huang, M.; Zeng, Y.; Yang, X.; Ying, Z.; Qin, G.; Shou, C.; Sheng, J.; Ye, J. Additive Engineering of the CuSCN Hole Transport Layer for High-Performance Perovskite Semitransparent Solar Cells. *ACS Appl. Mater. Interfaces* 2022, 14 (46), 52223−52232.

(51) Asuo, I. M.; Bouzidi, S.; Ka, I.; Rosei, F.; Pignolet, A.; Nechache, R.; Cloutier, S. G. All-Ambient-Processed CuSCN as an Inexpensive Alternative to Spiro-OMeTAD for Perovskite-Based Devices. *Energy Technology* 2021, 9 (1), No. 2000791.

(52) Cheng, J.; Hu, R.; Wang, K.; Meng, X.; Li, Y.; Yang, X.; Liao, X.; Li, L.; Chong, K. B. Air-Stable Solar Cells with 0.7 V Open-Circuit Voltage Using Selenized Antimony Sulfide Absorbers Prepared by Hydrazine-Free Solution Method. *Solar RRL* 2019, 3 (5), No. 1800346.

(53) Lee, S.-J.; Sung, S.-J.; Yang, K.-J.; Kang, J.-K.; Kim, J. Y.; Do, Y. S.; Kim, D.-H. Approach to Transparent Photovoltaics Based on Wide Band Gap Sb2S3 Absorber Layers and Optics-Based Device Optimization. *ACS Appl. Energy Mater.* 2020, 3 (12), 12644−12651.

(54) Im, S. H.; Lim, C.-S.; Chang, J. A.; Lee, Y. H.; Maiti, N.; Kim, H.-J.; Nazeeruddin, Md. K.; Grätzel, M.; Seok, S. I. Toward Interaction of Sensitizer and Functional Moieties in Hole-Transporting Materials for Efficient Semiconductor-Sensitized Solar Cells. *Nano Lett.* 2011, 11 (11), 4789−4793.

(55) You, M. S.; Lim, C.-S.; Kwon, D. H.; Heo, J. H.; Im, S. H.; Chae, K. J. Oxide-Free Sb2S3 Sensitized Solar Cells Fabricated by Spin and Heat-Treatment of Sb(III)(Thioacetamide)2Cl3. *Org. Electron.* 2015, 21, 155−159.

(56) Choi, Y. C.; Lee, D. U.; Noh, J. H.; Kim, E. K.; Seok, S. I. Highly Improved Sb2S3 Sensitized-Inorganic−Organic Heterojunction Solar Cells and Quantification of Traps by Deep-Level Transient Spectroscopy. *Adv. Funct. Mater.* 2014, 24 (23), 3587−3592.

(57) Peng, X.; Yang, J.; Zhao, Q.; Gao, H.; Huang, Y.; Wang, H.; Zhu, C.; Tang, R.; Chen, T. Negative-Pressure Sulfurization of Antimony Sulfide Thin Films for Generating a Record Open-Circuit Voltage of 805 mV in Solar Cell Applications. *J. Mater. Chem. A* 2023, 11 (36), 19298−19307.

(58) Demtsu, S. H.; Sites, J. R. Effect of Back-Contact Barrier on Thin-Film CdTe Solar Cells. *Thin Solid Films* 2006, 510 (1), 320−324.

(59) Yuan, S.; Deng, H.; Yang, X.; Hu, C.; Khan, J.; Ye, W.; Tang, J.; Song, H. Postsurface Selenization for High Performance Sb2S3 Planar Thin Film Solar Cells. *ACS Photonics* 2017, 4 (11), 2862−2870.

(60) Chan, D. S. H.; Phang, J. C. H. Analytical Methods for the Extraction of Solar-Cell Single- and Double-Diode Model Parameters from I-V Characteristics. *IEEE Trans. Electron Devices* 1987, 34 (2), 286−293.

(61) Wijeyasinghe, N.; Eisner, F.; Tsetseris, L.; Lin, Y.-H.; Seitkhan, A.; Li, J.; Yan, F.; Solomeshch, O.; Tessler, N.; Patsalas, P.; Anthopoulos, T. D. P-Doping of Copper(I) Thiocyanate (CuSCN) Hole-Transport Layers for High-Performance Transistors and Organic Solar Cells. *Adv. Funct. Mater.* 2018, 28 (31), No. 1802055.

(62) Moore, J. E.; Dongaonkar, S.; Chavali, R. V. K.; Alam, M. A.; Lundstrom, M. S. Correlation of Built-In Potential and I−V Crossover in Thin-Film Solar Cells. *IEEE Journal of Photovoltaics* 2014, 4 (4), 1138−1148.

(63) Qin, P.; Tanaka, S.; Ito, S.; Tetreault, N.; Manabe, K.; Nishino, H.; Nazeeruddin, M. K.; Grätzel, M. Inorganic Hole Conductor-Based Lead Halide Perovskite Solar Cells with 12.4% Conversion Efficiency. *Nat. Commun.* 2014, 5 (1), 3834.

(64) Liang, J.-W.; Firdaus, Y.; Azmi, R.; Faber, H.; Kaltsas, D.; Kang, C. H.; Nugraha, M. I.; Yengel, E.; Ng, T. K.; De Wolf, S.; Tsetseris, L.;

Ooi, B. S.; Anthopoulos, T. D. Cl2-Doped CuSCN Hole Transport Layer for Organic and Perovskite Solar Cells with Improved Stability. *ACS Energy Lett.* **2022**, 7 (9), 3139−3148.

(65) Zheng, J.; Liu, C.; Zhang, L.; Chen, Y.; Bao, F.; Liu, J.; Zhu, H.; Shen, K.; Mai, Y. Enhanced Hydrothermal Heterogeneous Deposition with Surfactant Additives for Efficient Sb2S3 Solar Cells. *Chemical Engineering Journal* **2022**, 446, No. 136474.

(66) Mao, Y.; Huang, L.; Zeng, W.-G.; Wu, F.-Y.; Yao, L.-Q.; Lin, L.-M.; Zhang, J.-M.; Li, J.-M.; Chen, G.-L. Bi Doping of Sb2S3 Light-Harvesting Films: Toward Suitable Energy Level Alignment and Broad Absorption for Solar Cells. *Chemical Engineering Journal* **2022**, 446, No. 137400.

(67) Savadogo, O.; Mandal, K. C. Low Cost Schottky Barrier Solar Cells Fabricated on CdSe and Sb2 S 3 Films Chemically Deposited with Silicotungstic Acid. *J. Electrochem. Soc.* **1994**, 141 (10), 2871.

(68) Kaienburg, P.; Hartnagel, P.; Pieters, B. E.; Yu, J.; Grabowski, D.; Liu, Z.; Haddad, J.; Rau, U.; Kirchartz, T. How Contact Layers Control Shunting Losses from Pinholes in Thin-Film Solar Cells. *J. Phys. Chem. C* **2018**, 122 (48), 27263−27272.

(69) Li, K.; Wang, S.; Chen, C.; Kondrotas, R.; Hu, M.; Lu, S.; Wang, C.; Chen, W.; Tang, J. 7.5% n−i−p Sb2Se3 Solar Cells with CuSCN as a Hole-Transport Layer. *J. Mater. Chem. A* **2019**, 7 (16), 9665−9672.